



Published in final edited form as:

Med Image Anal. 2014 April ; 18(3): 605–615. doi:10.1016/j.media.2014.02.001.

Automatic segmentation of intra-cochlear anatomy in post-implantation CT of unilateral cochlear implant recipients

Fitsum A. Reda^a, Theodore R. McRackan^b, Robert F. Labadie^b, Benoit M. Dawant^a, and Jack H. Noble^{a,*}

^aDepartment of Electrical Engineering and Computer Science, Vanderbilt University, Nashville, TN 37235, USA

^bDepartment of Otolaryngology-Head and Neck Surgery, Vanderbilt University Medical Center, Nashville, TN 37232, USA

Abstract

A cochlear implant (CI) is a neural prosthetic device that restores hearing by directly stimulating the auditory nerve using an electrode array that is implanted in the cochlea. In CI surgery, the surgeon accesses the cochlea and makes an opening where he/she inserts the electrode array blind to internal structures of the cochlea. Because of this, the final position of the electrode array relative to intra-cochlear anatomy is generally unknown. We have recently developed an approach for determining electrode array position relative to intra-cochlear anatomy using a pre- and a post-implantation CT. The approach is to segment the intra-cochlear anatomy in the pre-implantation CT, localize the electrodes in the post-implantation CT, and register the two CTs to determine relative electrode array position information. Currently, we are using this approach to develop a CI programming technique that uses patient-specific spatial information to create patient-customized sound processing strategies. However, this technique cannot be used for many CI users because it requires a pre-implantation CT that is not always acquired prior to implantation. In this study, we propose a method for automatic segmentation of intra-cochlear anatomy in post-implantation CT of unilateral recipients, thus eliminating the need for pre-implantation CTs in this population. The method is to segment the intra-cochlear anatomy in the implanted ear using information extracted from the normal contralateral ear and to exploit the intra-subject symmetry in cochlear anatomy across ears. To validate our method, we performed experiments on 30 ears for which both a pre- and a post-implantation CT are available. The mean and the maximum segmentation errors are 0.224 and 0.734 mm, respectively. These results indicate that our automatic segmentation method is accurate enough for developing patient-customized CI sound processing strategies for unilateral CI recipients using a post-implantation CT alone.

Keywords

Cochlear implant; Cochlear implant programming; Image registration; Surface-to-image registration; Statistical shape model

1. Introduction

A cochlear implant (CI) is a neural prosthetic device that restores hearing by directly stimulating the auditory nerve using an electrode array that is surgically implanted in the cochlea (U.S. Food and Drug Administration, 1995). An external sound processor, typically worn behind the ear, processes sounds detected by a microphone into signals sent to the implanted electrodes. The CI sound processor is programmed after implantation by an audiologist. Based on patient response, the audiologist determines stimulation levels for each electrode and selects a frequency allocation table to define which electrodes should be activated when specific sound frequencies are detected (Wilson et al., 1991). The number of electrodes in a CI electrode array ranges from 12 to 22, depending on the manufacturer.

CI electrode arrays are designed such that when optimally placed in the scala tympani cavity of the cochlea, each electrode stimulates regions of the auditory nerve corresponding to a pre-defined frequency bandwidth (Wilson and Dorman, 2008). However, because the surgeon threads the electrode array blind to internal cavities of the cochlea during the surgery, the final position of the electrode array relative to intra-cochlear anatomy is generally unknown. Research has shown that in 73% of CI surgeries the electrode array is placed fully within the scala tympani, while in the other 27% of CI surgeries, the electrode array is fully within a neighboring cavity or is initially inserted into the scala tympani but crosses into a neighboring cavity (Aschendorff et al., 2007). So far, the only option when programming the CI has been to assume the array is optimally placed in the cochlea and to use a default frequency allocation table. Currently, we are developing Image-Guided CI Programming (IGCIP) strategies that rely on patient-specific knowledge of the position of the electrodes relative to intra-cochlear anatomy, and we have shown that IGCIP strategies can significantly improve hearing outcomes (Noble et al., 2013). IGCIP strategies are enabled by a number of algorithms we have developed that permit determining the spatial relationship between intra-cochlear anatomy and the CI electrodes using a pre-implantation and a post-implantation CT (Noble et al., 2011a, 2011b, 2012; Schuman et al., 2010; Wanna et al., 2011). The intra-cochlear Structures-Of-Interest (SOIs) are the scala tympani (ST), scala vestibuli (SV), and the spiral ganglion (SG), which is the ganglion of auditory nerve bundles. 3D renderings of these structures as well as the implant are shown in Fig. 1a and b. Examples of pre- and post-implantation CTs with overlaid structure contours are shown in Fig. 1c and d.

The approach we previously developed for determining electrode array position relative to the SOIs involves several steps. First, we segment the SOIs in the pre-implantation CT. Next, we identify the electrode array in the post-implantation CT. Finally, we rigidly register the two CTs to determine the position of the electrodes relative to intra-cochlear anatomy. However, this approach cannot be used for many CI recipients because it requires a pre-implantation CT, which is not always acquired prior to implantation. Thus far, the pre-implantation rather than the post-implantation CT has been used to identify the SOIs because the cochlea is obscured by image artifacts introduced by the metallic electrode array in the post-implantation CT (see Fig. 1c and d). In this study, we propose methods to extend our IGCIP strategies to the population of unilateral CI recipients for whom a CT was not acquired pre-operatively, thereby increasing the portion of the population of existing CI

recipients who can benefit from IGCIP strategies. The methods we present permit automatic segmentation of the SOIs in the post-implantation CT despite the significant artifacts induced by the CI electrodes in those images.

2. Methods

The method we propose for segmenting the intra-cochlear anatomy of unilateral CI recipients takes advantage of the intra-subject inter-ear symmetry we have observed. We acquire a post-implantation CT in which both ears are in the field of view and segment the intra-cochlear anatomy of the implanted ear using information extracted from the normal contralateral ear. That is, we first segment in the normal contralateral ear the ST, SV, SG, which are the SOIs, and the labyrinth. The labyrinth, which we use as a landmark structure, externally bounds the intra-cochlear anatomy and includes the three semicircular canals (see Fig. 2). Next, we segment the SOIs in the implanted ear by projecting the SOI surfaces from the normal ear to the implanted ear. The transformation we use is the one that rigidly registers the mirrored labyrinth surface from the normal ear to the labyrinth in the implanted ear. The labyrinth provides adequate landmarks for this registration because a portion of the labyrinth lies far enough from the implant that its image features are not drastically affected by the implanted electrode array and, as we will show, the position of the labyrinth well predicts the position of the SOIs.

Our methods are detailed in the following subsections. In Section 2.1, we present details about our datasets. The registration processes we use at several steps throughout our work are detailed in Section 2.2. The study we perform to establish inter-ear symmetry of cochlear anatomy is presented in Section 2.3. The methods we use to segment both the labyrinth and the intra-cochlear anatomy in the normal ear are detailed in Section 2.4. Finally, in Section 2.5, we present the method we propose to segment the intra-cochlear anatomy in the implanted ear using information obtained from the normal ear.

2.1. Data

Table 1 summarizes the characteristics of the various sets of CT scans we have used. Age of subjects included in this study ranged from 18 to 90 years. The scans were acquired from several conventional scanners (GE BrightSpeed, LightSpeed Ultra; Siemens Sensation 16; and Philips Mx8000 IDT, iCT 128, and Brilliance 64) and a low-dose flat-panel volumetric CT (fpVCT) scanner (Xoran Technologies xCAT® ENT). Conventional CT scans of 10 subjects were used for symmetry analysis as described in Section 2.3; conventional CT scans of 18 subjects were used for active shape model (ASM) creation as discussed in Section 2.4.1; fpVCT scans of 14 subjects were used for intensity gradient model (IGM) creation as discussed in Section 2.5.2; and 18 CT-fpVCT pairs of scans were used for segmentation validation as discussed in Section 2.5.3. Typical scan resolution for conventional CT scans is $768 \times 768 \times 145$ voxels with $0.2 \times 0.2 \times 0.3$ mm³ voxel size. It is $700 \times 700 \times 360$ and $0.3 \times 0.3 \times 0.3$ or $0.4 \times 0.4 \times 0.4$ mm³ for fpVCT scans.

Dataset 4 is used for segmentation validation. Each implanted ear in the dataset will be automatically segmented in a post-implantation CT using the algorithms proposed in this paper. For each of these ears, there is a pre-implantation CT that is used to generate gold

standard segmentations to compare to the automatic segmentations for validation. Dataset 4 consists of two subgroups. The first (6 subjects) includes a set of conventional pre-implantation and low-dose post-implantation CTs of six unilateral CI recipients. The second (12 subjects) includes a set of conventional preimplantation and low-dose post-implantation CTs of a group of 12 bilateral CI recipients. We use the second set to increase the size of our testing set without having to scan more unilateral CI recipients prior to demonstrating the efficacy of our technique. To do so, we register the pre- and post-implantation CTs and use the contralateral side of the pre-implantation CT rather than the contralateral side of the post-implantation CT in our algorithm. Using this technique, we have 30 datasets (6 in the first group and 12×2 in the second group) on which we can test our unilateral segmentation algorithm. It should be noted that the second group of 24 ears from 12 subjects is not equivalent to ears from 24 subjects. While left and right ears generally have a different appearance in the post-implantation CT since the electrode array is positioned differently, differences in shape of anatomical structures between ears are not as large as inter-subject variations.

2.2. Image registration methods

Various processes we describe in the following subsections rely on image-to-image registration. In this subsection, we detail the affine and non-rigid registration methods we use. Given a “fixed” image, i.e., an atlas, and a “floating” image, i.e. the image we want to segment, we use a multi-step process outlined in Fig. 3 to register them. First, we affinely register the entire but downsampled images. Next, we refine the registration by limiting the region of interest to a pre-defined region that encompasses the ear structure. At this stage, the affine transformation is estimated at full resolution. In both cases, we rely on an intensity-based technique that uses Powell’s direction set method and Brent’s line search algorithm (Press et al., 1992) to optimize the mutual information (Wells et al., 1996; Maes et al., 1997) between the images. The registration within the region of interest is further refined with a non-rigid registration step using the adaptive-bases algorithm (ABA) (Rohde et al., 2003). ABA models the deformation field as a linear combination of a set of basis functions irregularly spaced over the image domain,

$$v(\mathbf{x}) = \sum_{i=1}^N c_i \Phi(\mathbf{x} - \mathbf{x}_i), \quad (1)$$

where x is a point in \mathbb{R}^d , with d being the dimensionality of images, the function Φ is Wu’s compactly supported positive definite radial basis function (Wu, 1995), and $\{c_i\}_{i=1}^N \in \mathbb{R}^d$ is the set of basis function coefficients that are selected to optimize the normalized mutual information (Studholme et al., 1999) between the images. The optimization process uses a gradient descent algorithm to determine the direction of optimization, and a line minimization algorithm to calculate the optimal step in that direction. The final deformation field is computed using a multiresolution and multiscale approach. Multiresolution is achieved by creating a standard image pyramid, and multiscale is achieved by modifying the region of support and the number of basis functions. A large region of support models a transformation at a large scale. The algorithm is initialized on a low-resolution image with few basis functions. Then, the region of support of the basis functions is reduced as the

algorithm progresses to finer resolutions and smaller scales (larger number of basis functions). Using this approach, the final deformation field is computed as

$$v(\mathbf{x}) = \sum_{k=1}^M \mathbf{v}_k(\mathbf{x}), \quad (2)$$

with M being the total number of combinations of scales and image resolutions used.

2.3. Symmetry analysis

To establish that the ST, SV, SG, and the labyrinth are symmetric across ears, we conduct experiments on the set of pre-implantation CTs in dataset 1 (see Table 1). We identify surfaces of the ST, SV, SG, and the labyrinth for both ears in each pre-implantation CT using methods that we describe in Section 2.4. Then, we register the surfaces of one ear to the corresponding surfaces of the contralateral ear using a standard point-based rigid-body registration method (Arun et al., 1987). Finally, we measure distances between the points on each surface to the corresponding points on the registered surface.

2.4. Segmentation of the normal ear

To segment the ST, SV, and SG in the normal ear, we use an automatic active shape model (ASM)-based method we have developed previously (Noble et al., 2013, 2011a). The mean and maximum surface errors in segmenting the ST in fpVCTs are 0.18 and 0.9 mm. These are 0.22 and 1.6 mm for the SV, and 0.15 and 1.3 mm for the SG, respectively.

The method we have developed for the automatic segmentation of the labyrinth relies on an active shape model. The following subsections describe how we create the model, how we use these models for segmentation purposes, and the study we have designed to test the accuracy of our results.

2.4.1. Labyrinth active shape model creation—We create an ASM of the labyrinth using the pre-implantation CTs in dataset 2 (see Table 1). We choose one of these pre-implantation CTs to serve as a reference volume, and we use the remaining CTs as training volumes. The active shape model creation process is outlined in Fig. 4. This process has six main steps. First, the labyrinth is segmented manually in the reference volume by an experienced otolaryngologist (TRM). Second, the training volumes are registered to the reference volume using the multi-step registration techniques described in Section 2.2. Third, the labyrinth in each of the training volumes are pre-segmented by projecting the labyrinth surface from the reference volume onto each of the training volumes using the transformations computed in step 2. Fourth, the surfaces produced in step 3 are manually edited to correct for possible segmentation errors caused by mis-registration. These four steps produce both segmented surfaces and a one-to-one point correspondence between points on the reference surface and points on each of the training surfaces. The procedures described in these four steps are similar to the approach described by Frangi et al. (2001). In the fifth step, all the training surfaces are registered to the reference surface with a 7-Degree-Of-Freedom (DOF) transformation (three rotations, three translations, and one isotropic scale) computed with a standard least squares fitting method (Arun et al., 1987).

We include isotropic scaling as a DOF so that inter-subject differences in labyrinth scale are normalized. Finally, in step (6), we use eigenanalysis to build the ASM, which is composed of the mean $\bar{\mathbf{x}}$ and the eigenvectors $\{\mathbf{u}_j\}$ of the covariance matrix \mathbf{X} of the registered shapes,

$$\{\lambda_j, \mathbf{u}_j\}_{j=0}^{M-2} : \lambda_j \mathbf{u}_j = \mathbf{X} \mathbf{u}_j, \quad (3)$$

where M is the number of training shapes and $\{\lambda_j\}$ is the set of eigenvalues (Cootes et al., 1995).

2.4.2. Segmentation of the labyrinth using the active shape model—Once an ASM of the labyrinth is built, we use it to segment the labyrinth in a target volume using the segmentation process outlined in Fig. 5. We start by registering the ASM reference volume to the target volume according to the procedure described in Section 2.2. We then project the ASM mean surface points onto the target volume and we fit the ASM to these projected points. This produces our initial segmentation that is then refined as follows. For each point on the ASM surface $\mathbf{y} = \{\mathbf{y}_i\}_{i=0}^{N-1}$ we find a new candidate point \mathbf{y}'_i by searching for the point with the highest image intensity gradient within the interval $[-1.35, 1.35]$ mm along the local surface normal $\hat{\mathbf{n}}_i$, equivalently,

$$\mathbf{y}'_i = \mathbf{y}_i + \Delta d \cdot k_{max} \cdot \hat{\mathbf{n}}_i,$$

where

$$k_{max} = \arg \max_k (I(\mathbf{y}_i + \Delta d \cdot (k+1) \cdot \hat{\mathbf{n}}_i) - I(\mathbf{y}_i + \Delta d \cdot (k-1) \cdot \hat{\mathbf{n}}_i)), \quad (4)$$

for $k \in [-9, 9]$ and $d = 0.15$ mm, where $I(\cdot)$ is the image intensity at a given point. The approach of finding a point with the maximum gradient is similar to those investigated by Kass et al. (1988), Staib and Duncan (1992), Cohen and Cohen (1993), Cootes et al. (1995), Chakraborty et al. (1996), and Sakalli et al. (2006). Then, we fit the ASM to the new

candidate point set $\mathbf{y}' = \{\mathbf{y}'_i\}_{i=0}^{N-1}$ to obtain an adjusted shape $\mathbf{y}'' = \{\mathbf{y}''_i\}_{i=0}^{N-1}$. To perform the fitting procedure, we first register \mathbf{y}' to the ASM mean shape $\bar{\mathbf{x}}$ with a 7-DOF (three rotations, three translations, and one isotropic scale factor) transformation ψ . Then, we compute the adjusted point set \mathbf{y}'' using the equation

$$\mathbf{y}''_i = \psi^{-1} \left(\bar{\mathbf{x}} + \sum_{j=0}^{K-1} b_j \mathbf{u}_{j,i} \right), \quad (5)$$

with K being the number of eigenshapes used, where

$$b_j = \mathbf{u}_j^T (\psi(\mathbf{y}') - \bar{\mathbf{x}}). \quad (6)$$

The magnitude of $\{b_j\}_{j=0}^{K-1}$ is chosen such that the Mahalanobis distance from the adjusted shape to the mean shape is less than 3:

$$\sqrt{\sum_{j=0}^{K-1} \left(\frac{b_j^2}{\lambda_j} \right)} \leq 3.$$

We iterate the adjustment step until the constraint $1/N \sum_{i=0}^{N-1} \|\mathbf{y}_i'' - \mathbf{y}_i\| < \varepsilon$ is satisfied, where N is the number of points, and ε is empirically set to 0.01 mm.

2.4.3. Labyrinth segmentation validation—To validate our labyrinth segmentation method, we fix the reference volume and use the method presented above to segment the remaining 17 training volumes in a leave-one-out approach. We measure distance between corresponding points on the automatic and manually generated surfaces to quantitatively evaluate the agreement between the two. Specifically, for each point on the automatic surface we measure the Euclidean distance to the corresponding point on the manual surface. Then, for each training volume, we measure the mean and maximum of these distances.

2.5. Segmentation of the implanted ear

The process we use to segment the intra-cochlear anatomy in an implanted ear is outlined in Fig. 6. In this process, we do not identify the intra-cochlear anatomy in the implanted ear directly. Rather, we identify the position of the labyrinth in the implanted ear and use it as a landmark structure to determine the position of the intra-cochlear anatomy. First, we estimate an initial position of the labyrinth in the implanted ear using a procedure described in Section 2.5.1. Next, we iteratively refine this estimation of the labyrinth position using a procedure described in Section 2.5.2. Finally, we determine the intra-cochlear anatomy in the implanted ear by projecting the intra-cochlear surfaces segmented in the normal ear through the transformation that rigidly registers the labyrinth from the normal ear to the iteratively refined labyrinth in the implanted ear. The following subsections detail this approach.

2.5.1. Segmentation initialization via image-to-image registration—To estimate an initial position of the labyrinth in the implanted ear, we project the labyrinth surface from the normal contralateral ear to the implanted ear. The transformation we use for projecting the labyrinth is the transformation that registers the normal ear to the implanted ear. Fig. 7 lists the steps we use to compute this transformation. We start by estimating a mirroring transformation through registration to a volume in which the mid-sagittal plane has been defined. Several approaches exist in the literature for accurate mid-sagittal plane extraction in MR images as well as other modalities (Rupper et al., 2011; Prima et al., 2002; Liu et al., 2001; Tuzikov et al., 2003, and Smith and Jenkinson, 1999). The approach we have selected, while likely not as accurate as these dedicated methods, requires little extra processing because registration with a reference is already performed prior to segmentation and provides an estimation of the mirroring transformation that is accurate enough to initialize a subsequent refinement step. This is achieved by computing a rigid body transformation with an intensity-based method applied first to the entire but downsampled images then to a

region of interest but at full resolution. This is similar to the process we use in the first step of the process described in Fig. 3.

2.5.2. Segmentation refinement via surface-to-image registration—To refine the position of the labyrinth, we iteratively adjust its position. We perform this by iteratively finding candidate positions for each point \mathbf{y}_i on the labyrinth surface and rigidly registering the surface to those candidate points. This is similar to the iterative closest point surface registration algorithm introduced by Besl and McKay (1992). At each iteration, we choose the candidate position \mathbf{y}'_i for each point \mathbf{y}_i as

$$\mathbf{y}'_i = \mathbf{y}_i + \Delta d \cdot k_{\min} \cdot \hat{\mathbf{n}}_i, \quad (7)$$

where $d = 0.15$ mm, and we choose k_{\min} to minimize the cost function

$$k_{\min} = \arg \min_k C_i(k) : k \in [-9, 9]. \quad (8)$$

The cost function $C_i(\bullet)$ we have designed for candidate selection at each i th point is a function of an intensity-gradient model (IGM) of the image at that point. To build the IGM, we rely on a set of manual segmentations of the labyrinth in dataset 3 (see Table 1). For each i th point on the j th training surface, $\{\mathbf{x}_{ji}\}_{i=0}^{N-1}$, we extract an intensity-gradient profile $g(\mathbf{x}_{ji})$ along the local normal $\hat{\mathbf{n}}_{ji}$ using the equation

$$\mathbf{g}(\mathbf{x}_{ji}) = \left[\left(I_j^{-10}(\mathbf{x}_{ji}) - I_j^{-8}(\mathbf{x}_{ji}) \right), \left(I_j^9(\mathbf{x}_{ji}) - I_j^{-7}(\mathbf{x}_{ji}) \right), \dots, \left(I_j^8(\mathbf{x}_{ji}) - I_j^{10}(\mathbf{x}_{ji}) \right) \right]^T, \quad (9)$$

where

$$I_j^k(\mathbf{x}_{ji}) = I_j(\mathbf{x}_{ji} + \Delta d \cdot k \cdot \hat{\mathbf{n}}_{ji}), \quad (10)$$

$d = 0.15$ mm, and $I_j(\bullet)$ is the intensity of the j th training image at a given point. Finally, we define the IGM as the set of $\{g(\mathbf{x}_{ji})\}_{i=0}^{N-1}$ for $j \in [0, 1, \dots, M-1]$, where N is the number of points composing each training surface, and M is the number of training surfaces.

The cost we use for candidate point selection in Eq. (8) above is then designed as

$$C_i(k) = \min_{j \in [0, 1, \dots, M-1]} \|\mathbf{g}(\mathbf{y}_i + \Delta d \cdot k \cdot \hat{\mathbf{n}}_i) - g(\mathbf{x}_{ji})\|, \quad (11)$$

which defines the cost for selecting $\mathbf{y}_i + \Delta d \cdot k \cdot \hat{\mathbf{n}}_i$ as a new candidate position for the i th point as the minimum Euclidean distance between the set of intensity-gradient profiles in the IGM and the intensity-gradient profile measured at that point. The standard approach is to compute the mean profile as well as the covariance of the profiles and determine candidate points by minimizing the Mahalanobis or Euclidean distance to the mean profile (Cootes et al., 1995; Cootes and Taylor, 2001; Mitchell et al., 2001; Heimann et al., 2006; Heimann and Meinzer, 2009; Brejl and Sonka, 2000; Tobon-Gomez et al., 2008). However, pilot

experiments we conducted indicated that our approach leads to superior final segmentation accuracy.

Finally, we compute the rigid body transformation T that registers the initial point set $\{\mathbf{y}_i\}$ to the candidate point set $\{\mathbf{y}'_i\}$ determined using Eq. (7) using a weighted least-squares approach (Sonka and Fitzpatrick, 2000), formulated as

$$\arg \min_T \sum_{i=0}^{N-1} w_i^2 \| (T(\mathbf{y}_i) - \mathbf{y}'_i) \|^2. \quad (12)$$

$\{w_i\}$ is a set of reliability weights that we assign to points using image intensity information derived from the images. Because the implant is very bright in the CT images, it obscures structure boundaries. Points that are near high intensity regions are thus assigned low weight values and points away from bright regions are assigned high weight values. To compute the weight values, we analyze the intensity distribution of the image over a subset of labyrinth boundary points that are known *a priori* to lie far away from the electrode (region shown in blue in Fig. 8) and use this information to create a weight function that estimates the likelihood that each labyrinth surface point is located near an electrode. To do this, we first extract intensity profiles $\mathbf{r}(z_i)$ at each i th point in the subset of surface points

$\{z_i\}_{i=0}^{N'-1} \subset \{\mathbf{y}_i\}_{i=0}^{N-1}$ that should lie far from the electrodes and is shown in blue in Fig. 8, using the equation

$$\mathbf{r}(z_i) = [I^{-10}(z_i), I^{-9}(z_i), \dots, I^{10}(z_i)]^T, \quad (13)$$

where

$$I^k(z_i) = I(z_i + \Delta d \cdot k \cdot \hat{\mathbf{n}}_i), \quad (14)$$

$d = 0.15$ mm, and $I(\bullet)$ is the intensity of the target image at a given point. Then, at each iteration of the registration process, we compute a weight for each point as

$$w_i = \begin{cases} 1.0 & \max(\mathbf{r}(\mathbf{y}_i)) < R \\ e^{-\frac{(\max(\mathbf{r}(\mathbf{y}_i)) - R)^2}{2\sigma^2}} & \max(\mathbf{r}(\mathbf{y}_i)) \geq R, \end{cases} \quad (15)$$

where the value of R is experimentally determined (see details below) to be the 68th percentile of the distribution of the maximum values of $\mathbf{r}(z_i)$ measured at $\{z_i\}_{i=0}^{N'-1}$, and σ is the standard deviation of the same distribution, computed as

$$\sigma = \left(\frac{1}{N'} \sum_{i=0}^{N'-1} (\max(\mathbf{r}(z_i)) - \mu)^2 \right)^{1/2}.$$

The weight function in Eq. (15) is designed such that a weight value of 1.0 is assigned to points with a maximum value in their intensity profile less than R , and weight values that

exponentially decay from 1.0 are assigned to points with a maximum value in their intensity profile greater than R . By assigning weights in this way, we achieve our goal, which is to constrain the registration to rely more on points located in regions that are less affected by the image artifacts produced by the implant.

The value of R , as defined above, is customized for each target image because the intensity distribution in the images generated by the low-dose scanner used in this study vary across patients. To arrive at the value of R , we use the set of testing image pairs in dataset 4. First, we sample R in increments of 4% percentiles in the distribution of maximum values of

intensities $\{max(\mathbf{r}(z_i))\}_{i=0}^{N'}$ and we measure the resulting SOI segmentation error on all testing image pairs. Next, we select the value of R as the value for which the overall mean segmentation error is the smallest. Fig. 9 shows a plot of the overall mean error for

$R \in \left[\min \left(\{max(\mathbf{r}(z_i))\}_{i=0}^{N'} \right) \max \left(\{max(\mathbf{r}(z_i))\}_{i=0}^{N'} \right) \right]$ in increments of 4 percentiles. As shown in this figure, $R = 68$ th percentile leads to the smallest segmentation error. This is the value, computed for each volume that is used to produce the results presented herein.

We iterate the surface-to-image registration step formulated in Eq. (12) until

$1/N \sum_{i=0}^{N-1} \|T(\mathbf{y}_i) - \mathbf{y}_i\| < \varepsilon$ is satisfied, where ε is empirically set to 0.01 mm. In summary, at each iteration, we determine candidate points $\{\mathbf{y}'_i\}$ using Eq. (7), we compute the weights $\{w_j\}$ using Eq. (15), and we register the initial points $\{\mathbf{y}_i\}$ to the candidate points $\{\mathbf{y}'_i\}$ using Eq. (12). Finally, we segment the intra-cochlear anatomy in the implanted ear by projecting the intra-cochlear surfaces from the normal ear to the implanted ear through the iteratively refined inter-ear labyrinth registration transformation.

2.5.3. Validation—We validate our method by automatically segmenting the post-implantation volumes in dataset 4 and measuring the resulting segmentation errors. The gold-standard surfaces that we use for comparison were created in the pre-implantation volumes by manually editing surface points on segmentations that are automatically initialized by our pre-implantation CT segmentation techniques. We measure distances between corresponding points on the automatic and gold standard surfaces to quantitatively evaluate the agreement between the two. Specifically, for each point on the automatic surface we measure the distance to the corresponding point on the gold standard surface. Then, for each volume, we measure the mean and maximum of the distances between all corresponding points. To assess how much improvement our proposed surface-to-image registration refinement step provides, we also measure segmentation errors achieved at initialization prior to performing the refinement step, which are the results that can be achieved using image registration alone. Finally we compare our technique to the best possible segmentation results that could be achieved using our contralateral ear registration method. These are obtained by registering directly the labyrinth surface in the normal ear to the gold standard labyrinth surface in the contralateral ear extracted from the pre-implantation CT with a 6-DOF (three rotations and three translations) point-based registration method that minimizes the RMS error between the two surfaces (Arun et al., 1987).

3. Results

3.1. Intra-cochlear anatomy and labyrinth symmetry

To demonstrate intra-subject inter-cochlear symmetry, we measured the distance between the ST, SV, and SG surfaces rigidly registered across ears in dataset 1. These measurements are presented in Table 2. Fig. 10 shows the ST, SV, and SG surfaces from one ear colormapped with the distance to the registered contralateral surface for subject one. These distance values are smaller than the segmentation error for these structures as reported in (Noble et al., 2013) and (Noble et al., 2011a). Distance maxima are located in the same areas segmentation error maxima occur, i.e., at both the apical and basal ends of the cochlea. Segmentation errors occur at these locations due to the relative scarcity of local information available in the CT image to estimate the location of the intra-cochlear structures in these regions. This suggests that the small differences between the registered contralateral segmentations seen in Fig. 10 are most likely due to segmentation error, and that the intra-cochlear anatomy is indeed highly symmetric.

We performed similar experiments to demonstrate the existence of intra-subject symmetry in labyrinth anatomy. We measured the distance between the labyrinth surfaces rigidly registered across ears in dataset 1. These measurements are presented in Table 3, and they are smaller than the labyrinth segmentation error reported in Section 3.2. These results suggest that the labyrinth is also highly symmetric.

3.2. Labyrinth segmentation in the normal ear

We built the ASM of the labyrinth using 18 pre-implantation CTs (see dataset 2 in Table 1). A total of 9100 points compose each labyrinth shape. Table 4 presents the percentage of shape variation captured by each of the first eight principal components. Table 4 presents the cumulative variations in percentage for the first nine principal components (eigenshapes). As shown in the table, the first nine principal components (eigenshapes) capture 90% of the shape variation in the training set. We used these eigenshapes in the ASM segmentation process. Previous studies suggest that the cochlea is fully formed at birth, and its size and shape does not change as an individual ages (Jeffery and Spoor, 2004). Thus, it is of note that the models we built are applicable for all age groups.

Table 5 presents the mean and maximum errors measured as the distance from each point on the automatically generated surface to the corresponding point on the manually generated surface. To illustrate the segmentation improvement provided by the ASM-based segmentation method, we also show errors for surfaces generated using an atlas-based segmentation method. In this approach we simply project the reference shape onto the target volume using the transformation that registers the reference volume to the target volume. The overall mean and maximum errors for the ASM-based segmentation method are 0.239 and 1.623 mm, respectively. These are 0.452 and 2.407 mm for the atlas-based method. The mean and maximum errors for the ASM-based method are smaller than the atlas-based method for all subjects.

In Fig. 11, we show renderings of the surfaces automatically segmented using both the ASM-based and atlas-based segmentation methods. These surfaces are colormapped with

the segmentation error. The top row in this figure shows the labyrinth of the subject with the smallest mean error (subject 16), and the bottom row shows the labyrinth with the largest mean error (subject 2). As can be seen, the surfaces generated using the atlas-based method have unnatural deformations, whereas the surfaces generated using the ASM-based method are smooth and resemble, as expected, the structure surfaces included in the ASM. As can also be seen in the figure, the mean errors for the ASM-based method are sub-millimetric over most of the labyrinth surface.

3.3. Intra-cochlear anatomy segmentation in the implanted ear

We compared quantitatively the gold-standard and automatically generated ST, SV, and SG surfaces for the 30 post-implantation ears in dataset 4. Fig. 12a shows box plots of the mean error for each SOI, and Fig. 12b shows the box plots of the maximum error for each SOI. In each box plot, the lower and upper bounds are the minimum and maximum values, respectively, the lower and upper whiskers are the first and third quartiles, respectively, and the red line is the second quartile or the median value. The overall mean and maximum errors for the proposed segmentation method are 0.224 and 0.734 mm, respectively. These results are comparable to those obtained by segmenting the SOIs in pre-implantation CT images using the methods described in (Noble et al., 2013, 2011a). In Fig. 13, we present qualitative results for the subject with the smallest maximum segmentation error (shown in green square on the box plots in Fig. 12) and for the subject with the largest maximum segmentation error (shown in red square on the box plots in Fig. 12). Gold standard contours are shown in red, blue, and green for ST, SV, and SG, respectively, and automatically generated contours are in yellow. For the subject with the smallest maximum error, there is excellent agreement between the gold-standard and automatic contours along the length of the structures. In the post-implantation CT, even though the structure boundary information is lost due to the presence of the implant, we are able to achieve sub-millimetric segmentation accuracy for all SOIs. For the subject with the largest maximum error, some disagreement between the gold-standard and automatic contours can be seen along the length of the structures. However, as shown in the surface visualization, these errors are still sub-millimetric. Fig. 13 suggests that a number of voxels in the immediate proximity to the electrode array (bright voxels) do not lie within the segmentation-delineated borders of the scala tympani/scala vestibuli. This is caused by beam hardening and partial volume reconstruction artifacts that make the electrode appear larger in the images than it really is as shown in Fig. 1.

Fig. 14a (left) shows the mean and maximum error box plots for all SOIs (pooled ST, SV, and SG) segmented using only the inter-ear image registration-based initialization method described in Section 2.5.1. The overall mean and maximum errors are 0.639 and 1.545 mm, respectively. Fig. 14a (middle) shows the mean and maximum error box plots for all SOIs segmented using the proposed method. As shown in the plots, using the proposed segmentation method leads to a 64.94% and 52.49% reduction in mean and maximum segmentation errors, respectively. Fig. 14a (right) shows box plots of mean and maximum errors for the best segmentation results that could be achieved using our proposed method, as described in Section 2.5.3. The overall mean and maximum errors are 0.166 and 0.657 mm, respectively. This shows that the segmentation results we achieve in post-implantation

CT are close to the best that are achievable, despite the lack of contrast in these images due to artifacts induced by the implanted electrode array. Fig. 14b shows the same information for the labyrinth.

4. Conclusion and discussion

Image-guided CI programming strategies like the ones we are currently developing require accurate localization of the position of implanted electrodes relative to intra-cochlear anatomy. Until now, it has been possible to segment the SOIs, localize the electrodes, and compute the distance between the electrodes and intra-cochlear anatomy only for CI recipients for whom a preimplantation CT has been acquired. In this work, we have presented a method that does not require a pre-implantation CT. Our approach is to segment the labyrinth in the contralateral normal ear and use its position to segment the SOIs in the implanted ear by exploiting the intra-subject inter-ear symmetry. We performed symmetry analysis on ten subjects and the results suggest that both the SOIs and the labyrinth are highly symmetric.

To the best of our knowledge, there have been no methods proposed to automatically segment the labyrinth with a high degree of accuracy. We validate the ASM-based method we propose on 17 ears using a leave-one-out approach. The overall mean and maximum errors are 0.239 and 1.623 mm, respectively. As shown in the SOI segmentation validation study on 30 subjects, this level of accuracy is sufficient to segment the SOIs with sub-millimetric accuracy. In previous work where we relied on a pre-implantation CT and achieved an average SOI segmentation error of 0.15 mm, we have obtained excellent programming results (Noble et al., 2013). The segmentation accuracy we achieve with the method presented in this article that does not require a pre-implantation CT is slightly larger (0.22 mm) but still small. We anticipate that this slight reduction in segmentation accuracy will not negatively affect the improvement in hearing outcomes we have observed in the more than 60 patients that have participated in our ongoing study (85% of these have reported substantial improvement in hearing). However, we will only be able to confirm this after we have assessed hearing improvements in subjects for whom a pre-operative CT has not been acquired and a programming plan has been created using only a post-implantation CT and the method described herein.

We note that the proposed approach does not permit us to identify intra-cochlear anatomy for bilateral implant users for whom a pre-implantation CT has not been acquired. We are currently expanding our segmentation techniques (Reda et al., 2014) to make it possible and thus provide all cochlear implant subjects access to our image-guided programming method.

Acknowledgments

This work was supported by NIH Grants R01DC008408, R21DC012620, and R01DC010184 from the National Institute on Deafness and Other Communication Disorders. The content is solely the responsibility of the authors and does not necessarily represent the official views of this institute. We would also like to thank the reviewers for their detailed comments and suggestions, which have helped improve the quality of this article.

References

- Arun KS, Huang TS, Blostein SD. Least-squares fitting of two 3-D point sets. *IEEE Trans. Pattern Anal. Mach. Intell.* 1987; 9(5):698–700. [PubMed: 21869429]
- Aschendorff A, Kromeier J, Klenzner T, Laszig R. Quality control after insertion of the nucleus contour and contour advance electrode in adults. *Ear Hearing.* 2007; 28:75S–79S. [PubMed: 17496653]
- Besl PJ, McKay HD. A method for registration of 3-D shapes. *IEEE Trans. Pattern Anal. Mach. Intell.* 1992; 14(2):239–256.
- Brej1 M, Sonka M. Object localization and border detection criteria design in edge-based image segmentation: automated learning from examples. *IEEE Trans. Med. Imaging.* 2000; 19(10):973–985. [PubMed: 11131495]
- Chakraborty A, Staib L, Duncan JS. Deformable boundary finding in medical images by integrating gradient and region information. *IEEE Trans. Med. Imaging.* 1996; 15(6):859–870. [PubMed: 18215965]
- Cohen L, Cohen I. Finite-element methods for active contours models and balloons for 2-D and 3-D images. *IEEE Trans. Pattern Anal. Mach. Intell.* 1993; 15(11):1131–1147.
- Cootes TF, Taylor CJ, Sonka M, Hanson KM. Statistical models of appearance for medical image analysis and computer vision. *Proceedings of the SPIE Medical Imaging.* 2001; 4322:236–248.
- Cootes TF, Taylor CJ, Cooper DH, Graham J. Active shape models – their training and application. *Comput. Vis. Image Understan.* 1995; 61(1):39–59.
- Frangi, Niessen WJ, Viergever MA. Three-dimensional modeling for functional analysis of cardiac images: a review. *IEEE Trans. Med. Imaging.* 2001; 20(1):2–25. [PubMed: 11293688]
- Heimann T, Meinzer H-P. Statistical shape models for 3D medical image segmentation: a review. *Med. Image Anal.* 2009; 13(4):543–563. [PubMed: 19525140]
- Heimann, T.; Wolf, I.; Meinzer, H-P. Active shape models for a fully automated 3D segmentation of the liver – an evaluation on clinical data. In: Larsen, R.; Nielsen, M.; Sporning, J., editors. *Proceeding of MICCAI, LNCS.* Vol. 4191. Springer; 2006. p. 41-48.
- Jeffery N, Spoor F. Prenatal growth and development of the modern human labyrinth. *J. Anat.* 2004; 204:71–92. [PubMed: 15032915]
- Kass M, Witkin A, Terzopoulos D. Snakes: active contour models. *Int. J. Comput. Vision.* 1988; 1(4): 321–331.
- Liu Y, Collins RT, Rothfus WE. Robust midsagittal plane extraction from normal and pathological 3D neuroradiology images. *IEEE Trans. Med. Imaging.* 2001; 20(3):175–192. [PubMed: 11341708]
- Maes F, Collignon A, Vandermeulen D, Mrchal G, Suetens P. Multimodality image registration by maximization of mutual information. *IEEE Trans. Med. Imaging.* 1997; 16(2):187–198. [PubMed: 9101328]
- Mitchell SC, Lelieveldt BPF, van der Geest RJ, Bosch HG, Reiber JHC, Sonka M. Multistage hybrid active appearance model matching: segmentation of left and right ventricles in cardiac MR images. *IEEE Trans. Med. Imaging.* 2001; 20(5):415–423. [PubMed: 11403200]
- Noble JH, Labadie RF, Majdani O, Dawant BM. Automatic segmentation of intracochlear anatomy in conventional CT. *IEEE Trans. Biomed. Eng.* 2011a; 58(9):2625–2632. [PubMed: 21708495]
- Noble, Jack H, Schuman, Theodore A, Wright, Charles G, Labadie, Robert F, Dawant, Benoit M. Automatic identification of cochlear implant electrode arrays for post-operative assessment. *Proceedings of the SPIE 7962(796217), Medical, Imaging.* 2011b 2011b.
- Noble JH, Gifford RH, Labadie RF, Dawant BM. Statistical shape model segmentation and frequency mapping of cochlear implant stimulation targets in CT. *MICCAI.* 20122012:421–428. [PubMed: 23286076]
- Noble JH, Labadie RF, Gifford RH, Dawant BM. Image-guidance enables new methods for customizing cochlear implant stimulation strategies. *IEEE Trans. Neural Syst. Rehabil. Eng.* 2013; 21(5):820–829. [PubMed: 23529109]
- Press, WH.; Flannery, BP.; Teukolsky, SA.; Vetterling, WT. *Numerical Recipes in C.* second ed. Cambridge University Press; Cambridge: 1992. p. 412-419.

- Prima S, Ourselin S, Ayache N. Computation of the mid-sagittal plane in 3-D brain images. *IEEE Transactions on Medical Imaging*. Feb.2002 2002 21(no. 2):122, 148. [PubMed: 11929100]
- Reda, Fitsum A, Noble, Jack H, Labadie, Robert F, Dawant, Benoit M. An artifact-robust, shape library-based method for automatic segmentation of inner-ear anatomy in post-cochlear-implantation CT. *Proceedings of the SPIE 9034(9034-103), Medical, Imaging*. 20142014
- Rohde GK, Aldroubi A, Dawant BM. The adaptive bases algorithm for intensity-based nonrigid image registration. *IEEE Trans. Med. Imaging*. 2003; 22(11):1470–1479. [PubMed: 14606680]
- Ruppert GCS, Teverovisky L, Chen-Ping Yu, Falaco AX, Yanxi Liu. A new symmetry based method for mid-sagittal plane extraction in neuroimages. 2011 IEEE International Symposium on Biomedical Imaging: From Nano to Macro. 2011:285–288.
- Sakalli M, Lam K-M, Yan H. A faster converging snake algorithm to locate object boundaries. *IEEE Trans. Image Process*. 2006; 15(5):1182–1191. [PubMed: 16671299]
- Schuman TA, Noble JH, Wright CG, Wanna GB, Dawant BM, Labadie RF. Anatomic verification of a novel, non-rigid registration method for precise intrascalar localization of cochlear implant electrodes in adult human temporal bones using clinically-available computerized tomography. *The Laryngoscope*. 2010; 120(11):2277–2283. [PubMed: 20939074]
- Smith, SM.; Jenkinson, M. *Proc. MICCAI '99*. Springer-Verlag; London, UK: 1999. 1999. Accurate robust symmetry estimation; p. 308-317.
- Sonka M, Fitzpatrick JM. *Medical image processing and analysis. Handbook Med. Imaging*. 2000; 2:369–370. (Chapter 8).
- Staib LH, Duncan JS. Boundary finding with parametrically deformable models. *IEEE Trans. Pattern Anal. Mach. Intell*. 1992; 14(11):1061–1075.
- Studholme C, Hill DLG, Hawkes DJ. An overlap invariant entropy measure of 3D medical image alignment. *Pattern Recogn*. 1999; 32(1):71–86.
- Tobon-Gomez C, Butakoff C, Aguade S, Sukno F, Moragas G, Frangi AF. Automatic construction of 3D-ASM intensity models by simulating image acquisition: application to myocardial gated SPECT studies. *IEEE Trans. Med. Imaging*. 2008; 27(11):1655–1667. [PubMed: 18955180]
- Tuzikov AV, Colliot O, Bloch I. Evaluation of the symmetry plane in 3D MR brain images. *Pattern Recogn. Lett*. 2003; 24(14):2219–2233.
- U.S. Food and Drug Administration PMA. Cochlear implantation, No. 84002446. Aug 21.1995
- Wanna GB, Noble JH, McRackan TR, Dawant BM, Dietrich MS, Watkins LD, Rivas A, Schuman TA, Labadie RF. Assessment of electrode positions and audiological outcomes in bilateral cochlear implant patients. *Otol. Neurotol*. 2011; 32(3):428–432. [PubMed: 21283037]
- Wells WM III, Viola P, Atsumi H, Nakajima S, Kikinis R. Multi-modal volume registration by maximization of mutual information. *Med. Image Anal*. 1996; 1(1):35–51. [PubMed: 9873920]
- Wilson BS, Dorman MF. Cochlear implants: current designs and future possibilities. *J. Rehab. Res. Dev*. 2008; 45(5):695–730.
- Wilson BS, Finley CC, Lawson DT, Wolford RD, Eddington DK, Rabinowitz WM. Better speech recognition with cochlear implants. *Nature*. 1991; 352:236–238. [PubMed: 1857418]
- Wu Z. Multivariate compactly supported positive definite radial basis functions. *Adv. Comput. Math*. 1995; 4:283–292.

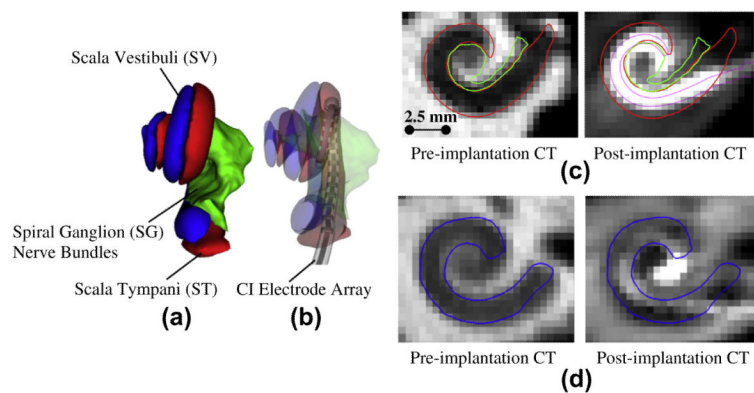


Fig. 1. Shown in (a) and (b) are surfaces of ST (red), SV (blue), and SG (green). In (b), a surface model of a CI electrode array inserted into ST is shown. In (c), contours of ST (red), SG (green) and the electrodes (purple) in the coronal view of a pre-implantation CT and a corresponding post-implantation CT, and in (d) contours of the SV (blue) in the coronal view of a pre-implantation CT and a corresponding post-implantation CT. The bright structure in the post-implantation CTs is the artifact cause by the CI electrode array. (For interpretation of the references to color in this figure legend, the reader is referred to the web version of this article.)

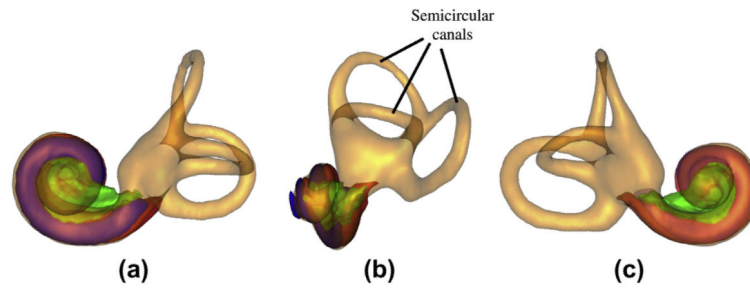


Fig. 2. Surfaces of the labyrinth (shown in transparent gold) and intra-cochlear anatomy (shown in transparent red (ST), transparent blue (SV), and transparent green (SG)) viewed in three orientations (a), (b), and (c). (For interpretation of the references to color in this figure legend, the reader is referred to the web version of this article.)

- (1) Affine registration
 - a. Affinely register the floating image to the fixed image, after downsampling both images by a factor of four in each dimension.
 - b. Crop the ear region from the affinely registered floating image
 - c. Affinely register the floating ear region to the fixed ear region image at full image resolution.
- (2) Non-rigid registration
 - a. Non-rigidly register the floating ear region to the fixed ear region image.

Fig. 3.
Image registration process.

- (1) Manually segment the labyrinth in a reference volume.
- (2) Register the training volumes to the reference volume (see Section 2.2)
- (3) Pre-segment automatically the labyrinth in the training volumes by projecting the reference surface onto the training volumes with the transformations computed in step 2.
- (4) Manually adjust the surfaces produced automatically
- (5) Register the labyrinth surfaces in the training volumes to the reference surface
- (6) Build an active shape model using the eigenanalysis method.

Fig. 4.
Active shape model generation process.

- (1) Automatically initialize shape
 - a. Register reference volume to target volume
 - b. Project ASM mean shape to the target volume space and fit the ASM to the projected points
- (2) Adjust shape
 - a. Find a candidate point along each point's normal
 - b. Fit the ASM to the candidate point set
- (3) Iterate (2) until convergence

Fig. 5.
Active shape segmentation process.

- (1) Automatically initialize the position of the labyrinth
 - a. Rigidly register the normal ear to the implanted ear
 - b. Project the labyrinth surface from the normal ear to the implanted ear
- (2) Adjust the labyrinth surface
 - a. Find a candidate point along each point's normal
 - b. Assign a weight to each point
 - c. Rigidly register initial point set to candidate point set
- (3) Iterate (2) until convergence
- (4) Project intra-cochlear surfaces from normal ear to implanted ear

Fig. 6.
Iterative intra-cochlear anatomy segmentation process.

- (1) Initialize a mirroring (inter-ear registration) transformation
 - a. Rigidly register the target image to an atlas image where the mid-sagittal plane is pre-defined.
 - b. Mirror the target image along the pre-defined plane.
 - c. Project the mirrored image back onto the original target image space
- (2) Refine the mirroring transformation
- (3) Project the labyrinth surface from the normal ear to the implanted ear.

Fig. 7.
Inter-ear registration process.

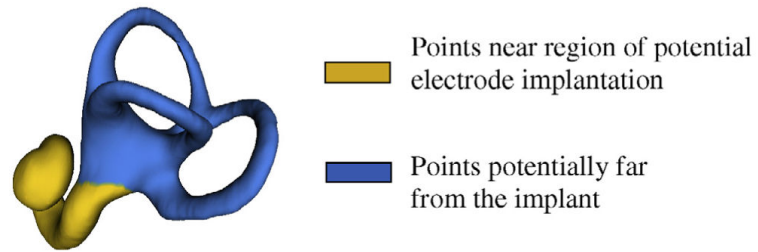


Fig. 8.

Points shown in blue are the points we use for computing R , the main parameter in our weight function. The remaining points of the labyrinth surface are shown in yellow. (For interpretation of the references to color in this figure legend, the reader is referred to the web version of this article.)

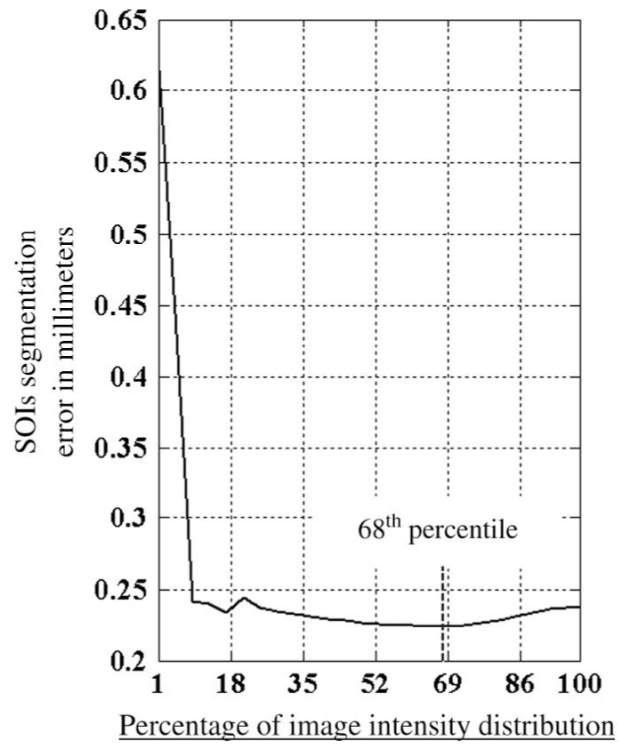


Fig. 9.
Mean error in the SOIs versus selection of R as a function of image intensity.

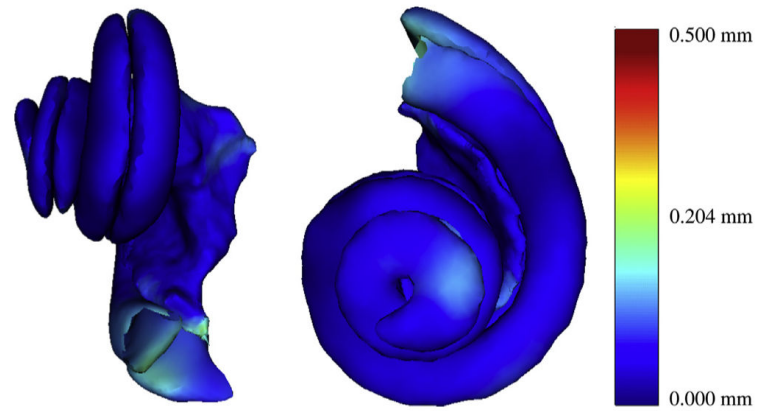


Fig. 10.

Subject one's ST, SV, and SG surfaces viewed in two different orientations. The color at each point encodes the distance in mm to the corresponding point on the registered contralateral surfaces. (For interpretation of the references to color in this figure legend, the reader is referred to the web version of this article.)

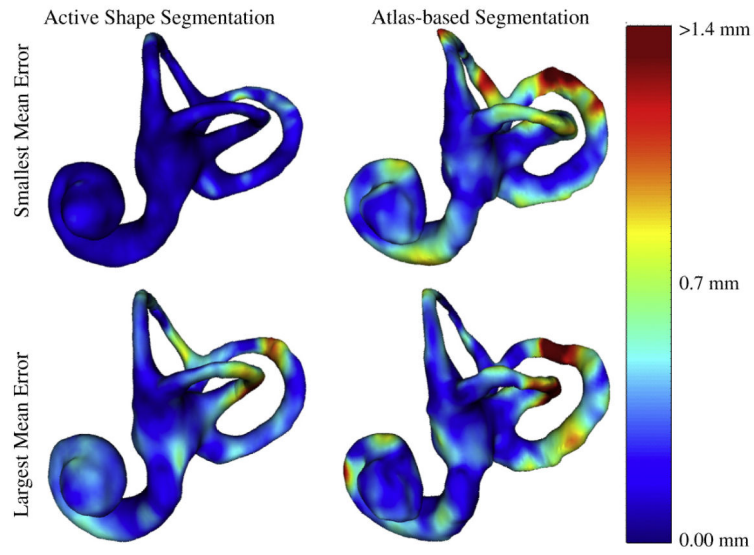


Fig. 11. Automatically generated surfaces colormapped with errors in mm for subject 16 (top row) and subject 2 (bottom row). Left, surface of the labyrinth generated by the ASM-based method; right surface of the labyrinth generated by the atlas-based method. (For interpretation of the references to color in this figure legend, the reader is referred to the web version of this article.)

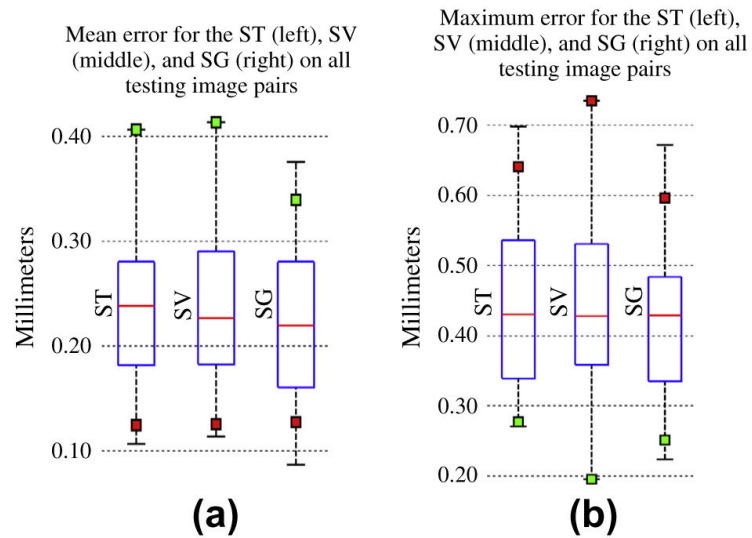


Fig. 12. Quantitative results for the proposed segmentation method. The green squares on the box plots are quantitative results for the subject with the smallest maximum error, and the red squares are quantitative results for the subject with the largest maximum error. (For interpretation of the references to color in this figure legend, the reader is referred to the web version of this article.)

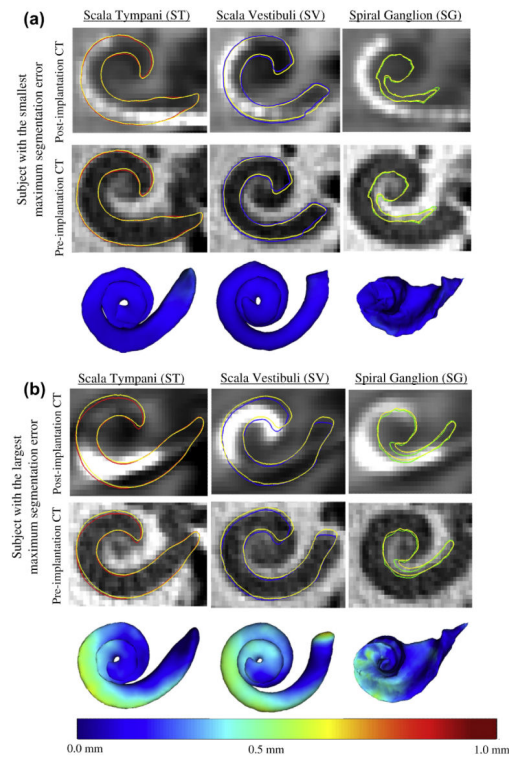


Fig. 13.

Qualitative segmentation results for the case with the smallest maximum segmentation error (shown in green box on Fig. 12). The contours shown are the ST (left panel), SV (middle panel), SG (right panel). Structure contours for gold-standard ST (red), gold-standard SV (blue), gold-standard SG (green), and automatic contours for all structures (yellow) are shown in a slice of a post-implantation image (top row) and a corresponding pre-implantation image (middle row). On the bottom panels the structure surfaces colormapped with segmentation errors are shown. (b) Shows similar information for the subject with the largest maximum segmentation error (shown in red box on Fig. 12). (For interpretation of the references to color in this figure legend, the reader is referred to the web version of this article.)

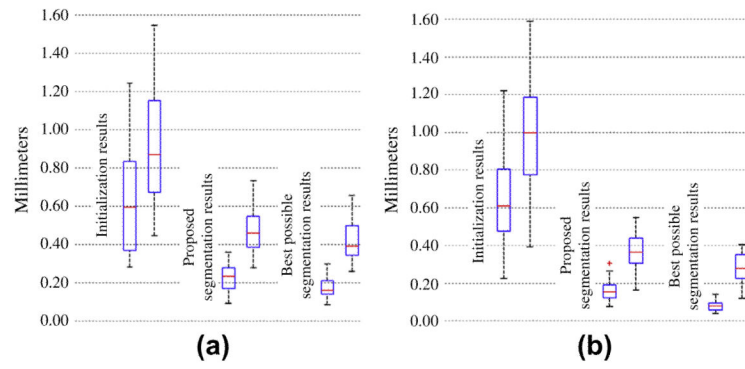


Fig. 14.

Various quantitative segmentation results for all 30 testing post-implantation CTs. (a) Mean and maximum error box plots for the SOIs segmented using the initialization method (left), using the proposed segmentation method (middle). On the right are the mean and maximum error box plots for the best possible SOIs segmentation results. (b) Shows the same information for the labyrinth.

Table 1

Datasets used in this study.

Dataset #	Purpose	Dataset size	Acquisition		# Of CIs		
			Xoran fpVCT	Conventional	No CIs	One CI	Two CIs
1	Symmetry analysis	10		×	×		
2	ASM creation	18		×	×		
3	IGM creation	14	×		×		
4	Segmentation validation	6		×	×		
		12	×	×	×	×	
			×				×

Author Manuscript

Author Manuscript

Author Manuscript

Author Manuscript

Table 2

Distances in millimeter between rigidly registered ST, SV and SG surfaces.

Subjects	<u>Scala Tympani (ST)</u>		<u>Scala Vestibuli (SV)</u>		<u>Spiral Ganglion (SG)</u>	
	Mean	Maximum	Mean	Maximum	Mean	Maximum
1	0.099	0.287	0.088	0.243	0.092	0.350
2	0.051	0.159	0.054	0.108	0.064	0.159
3	0.019	0.071	0.018	0.054	0.030	0.113
4	0.049	0.121	0.044	0.133	0.046	0.118
5	0.059	0.160	0.059	0.161	0.063	0.245
6	0.063	0.144	0.055	0.155	0.073	0.212
7	0.087	0.328	0.064	0.164	0.065	0.162
8	0.049	0.115	0.045	0.119	0.067	0.193
9	0.055	0.139	0.050	0.142	0.049	0.160
10	0.058	0.176	0.058	0.140	0.068	0.172
Overall	0.059	0.328	0.054	0.243	0.062	0.350

Table 3

Distances in millimeter between rigidly registered labyrinth surfaces.

Subject	1	2	3	4	5	6	7	8	9	10	Overall
Mean (mm)	0.100	0.064	0.082	0.073	0.051	0.094	0.071	0.053	0.120	0.039	0.075
Maximum (mm)	0.239	0.226	0.276	0.264	0.171	0.348	0.329	0.185	0.320	0.140	0.348

Table 4

Percent of labyrinth shape variations captured by the principal components of the shapes used for building the ASM of the labyrinth.

Principal component	1	2	3	4	5	6	7	8	9
Cumulated variations %	25.07	42.98	55.02	66.64	74.31	78.95	83.21	87.08	90.00

Author Manuscript

Author Manuscript

Author Manuscript

Author Manuscript

Table 5
Mean and maximum labyrinth segmentation errors in mm for both atlas-based and ASM-based methods.

		Subjects								
		1	2	3	4	5	6	7	8	9
Atlas-based method	Mean	0.442	0.408	0.395	0.370	0.458	0.414	0.534	0.616	0.489
	Maximum	2.153	2.156	1.757	1.450	2.140	2.009	2.407	2.299	1.536
ASM-based method	Mean	0.254	0.335	0.236	0.280	0.240	0.256	0.174	0.232	0.238
	Maximum	0.963	1.623	1.017	0.679	1.123	1.223	0.664	1.398	0.993
		10	11	12	13	14	15	16	17	Overall
Atlas-based method	Mean	0.483	0.451	0.376	0.494	0.445	0.385	0.427	0.495	0.452
	Maximum	2.366	1.516	1.358	1.978	1.883	1.456	1.819	1.574	2.407
ASM-based method	Mean	0.162	0.286	0.239	0.231	0.336	0.273	0.132	0.160	0.239
	Maximum	0.663	1.145	1.391	0.912	1.078	0.975	0.917	0.904	1.623